

# Photonic Snake States in Two-Dimensional Frequency Combs

Salim B. Ivars,<sup>1,2</sup> Yaroslav V. Kartashov,<sup>3,4</sup> P. Fernández de Córdoba,<sup>1</sup> J. Alberto Conejero,<sup>1</sup> Lluís Torner,<sup>3,5</sup> and Carles Milián<sup>1,\*</sup>

<sup>1</sup>*Institut Universitari de Matemàtica Pura i Aplicada,  
Universitat Politècnica de València, 46022 València, Spain*

<sup>2</sup>*Departament de Física, Universitat Politècnica de Catalunya, 08222 Terrassa (Barcelona), Spain*

<sup>3</sup>*ICFO–Institut de Ciències Fotòniques, The Barcelona Institute of  
Science and Technology, 08860 Castelldefels (Barcelona), Spain*

<sup>4</sup>*Institute of Spectroscopy, Russian Academy of Sciences, Troitsk, Moscow, 108840, Russia*

<sup>5</sup>*Universitat Politècnica de Catalunya, 08034 Barcelona, Spain*

**Taming the instabilities inherent to many nonlinear optical phenomena is of paramount importance for modern photonics. In particular, the so-called snake instability is universally known to severely distort localized wave stripes, leading to the occurrence of transient, short-lived dynamical states that eventually decay. The phenomenon is ubiquitous in nonlinear science, from river meandering to superfluids, and to date it remains apparently uncontrollable. However, here we show that optical snake instabilities can be harnessed by a process that leads to the formation of stationary and robust two-dimensional zigzag states. We find that such new type of nonlinear waves exists in the hyperbolic regime of cylindrical micro-resonators and it naturally corresponds to two-dimensional frequency combs featuring spectral heterogeneity and intrinsic synchronization. We uncover the conditions of the existence of such spatiotemporal photonic snakes and confirm their remarkable robustness against perturbations. Our findings represent a new paradigm for frequency comb generation, thus opening the door to a whole range of applications in communications, metrology, and spectroscopy.**

Since their discovery almost half a century ago, the so-called flexural instabilities [1], which lead to the unarrestable decay of quasi-one-dimensional self-sustained states such as solitons [2, 3], have been encountered in all areas of nonlinear sciences. Namely, they have been found to occur in the dynamics of river meandering [4], classical fluids [5], fermion [6, 7] and polariton [8] superfluids, Bose-Einstein condensates [9], chemistry [10], and, importantly, nonlinear photonics [11–15]. The initial stages of the instability – referred to as the *snake* instability [2] – evinces the reshaping of straight states into zigzags caused by spontaneous and local transverse drifts with alternating directions, which occur prior to the irreversible decay of the corresponding states. In contrast to the use of the instability in several systems, e.g., to trigger spontaneous vortex formation [9, 11, 12], its controlled arrest to form robust multi-dimensional snaking states remains hitherto unexpected.

In parallel, in recent years, microring cavities have emerged as an outstanding platform for exploring the fundamental properties and the applications of stabilised one-dimensional dissipative nonlinear waves, in both the normal and the anomalous dispersion regimes, under a plethora of potentially unfavourable situations, such as strong dispersive [16, 17], inelastic [18–20], and thermal [21, 22] effects. Each and every new solitonic states found in such micron-sized systems correspond to highly stable frequency combs that contribute to the developing field of comb-related applications [23, 24]. As a conse-

quence, microring-like cavities are highly appealing systems to push the frontiers of knowledge of nonlinear phenomena as well as boosting applications in photonics. Nowadays, most solitonic states (stable combs) that have been experimentally observed in microrings occur in essentially single-comb forming devices, except for the few exceptions that may be found in counter-propagating soliton experiments [25, 26], in systems with two microrings [27, 28], or in cavities with a few transverse modes [29], where each of the individual combs are formally one-dimensional. The potential of two-dimensional frequency combs, which to date is essentially unexplored experimentally, remains to be uncovered.

Here we discover the existence of robust spatiotemporal photonic snakes in cylindrical micro-resonators with normal group velocity dispersion (GVD) and in the presence of diffraction along the cylinder’s axis. Such previously unknown states are a continuous two-dimensional ensemble of heterogeneous combs which are inherently synchronised by the nonlinearity. Thus, they represent a whole new paradigm for frequency comb formation.

## Results

**Model.** The spatiotemporal snakes predicted here form in hollow cylindrical Kerr micro-resonators [cf. Fig. 1a]. The dynamics of the intra-cavity field can be accurately described by the two-dimensional generalisation of the Lugiato-Lefever equation [30],

$$\partial_t \psi = \frac{i}{2} (-\partial_x^2 + \partial_z^2) \psi - (1 + i\delta) \psi + i|\psi|^2 \psi + i h_0 e^{-z^2/\sigma_z^2}, \quad (1)$$

where the terms on the right-hand side of the equation

\* carmien@upvnet.upv.es

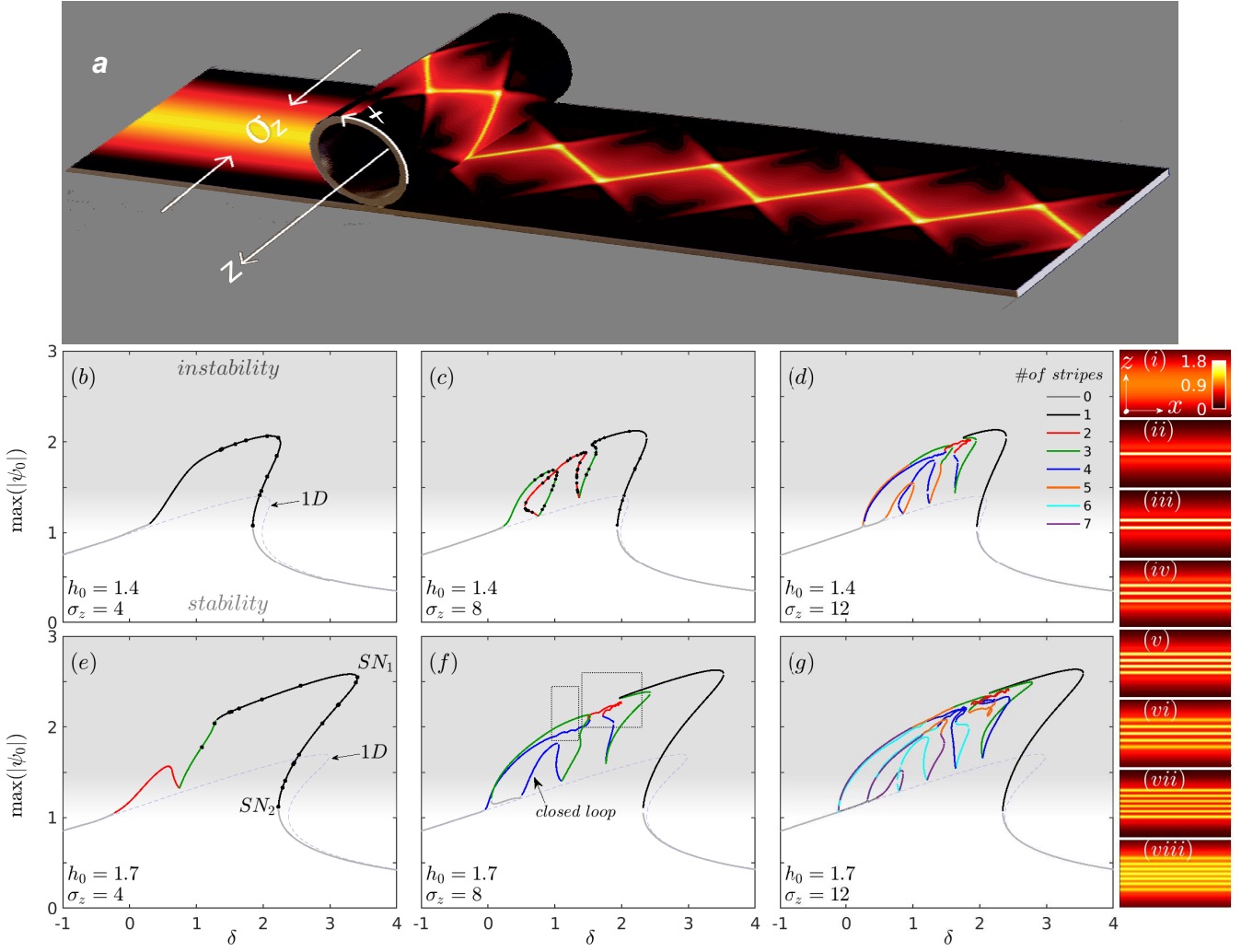


FIG. 1. | **Cylindrical microresonator and multi-stable resonances.** **a**, sketch of the driven (from the left) micro-cylinder in the photonic snake regime. **b-g**, maximum of the cavity background (single color) field amplitude,  $|\psi_0(x, z)|$ , versus laser-cavity detuning,  $\delta$ , showing selected nonlinear resonances for driving strengths **b-d**  $h_0 = 1.4$ , **e-g**  $h_0 = 1.7$ , and various values of the transverse pump width: **b,e**  $\sigma_z = 4$ ; **c,f**  $\sigma_z = 8$ ; **d,g**  $\sigma_z = 12$ . The cavity background may be smooth [inset (i)] or may feature single- and multi-stripe quasi one-dimensional solitons distributed along  $z$  [insets (ii) – (viii)]. The number of stripes on each portion of the resonances is colour coded in the legend of **d**. The resonance corresponding to the *one-dimensional* microring is also shown, for reference, by the dashed curves labeled as ‘1D’ in **b, e**. Thick black dots on the resonances in **b,c,e** mark the onsets of instabilities and correspond to bifurcation points for spatiotemporal states, including snakes [see Fig.2]. Labels  $SN_{1,2}$  in **e** mark the saddle node bifurcations (branch turning points) further discussed in Fig.3. Rectangles in **f** enclose the regions zoomed in Figs.4b and 4e. Background states are stable for  $|\psi_0| < 1$  and may be unstable otherwise, within the grey shaded areas. Insets showing spatial profiles are plotted over the area  $x \in [-L/2, L/2[$  (covering the whole cavity length,  $L = 16$ ) and  $z \in [-16, 16]$ .

account for normal GVD along the propagation (and periodic) coordinate, diffraction along the cylinder’s axis, losses, laser-cavity detuning, focusing nonlinearity, and the axially localised pump, respectively (see methods). For the sake of generality, we discuss photonic snakes first in the physical frame of Eq.1 [cf. Figs. 1-5], which represents a universal hyperbolic model governing a plethora of nonlinear physical phenomena in optics [31, 32] and other areas of physics [33]. In order to anchor our predictions into realistic optical frequency comb forming experimental realizations, we report on the snakes’ robustness

under the specific collection of perturbations expected in cylindrical micro-cavities [cf. Fig. 6], including Raman and thermal nonlinearities, among others (see methods).

**Nonlinear resonances.** When driven into the strongly nonlinear regime, the here considered micro-cylinders develop nonlinear resonances, associated to the single colour locked states,  $\psi_0$  ( $\partial_t \psi_0 = \partial_x \psi_0 = 0$ ), exhibiting an unusually rich multi-stability landscape, as shown in Figs.1b-g. For peak intensities  $|\psi_0| \gtrsim 1$ , corresponding to the existence domain of bright solitons with anoma-

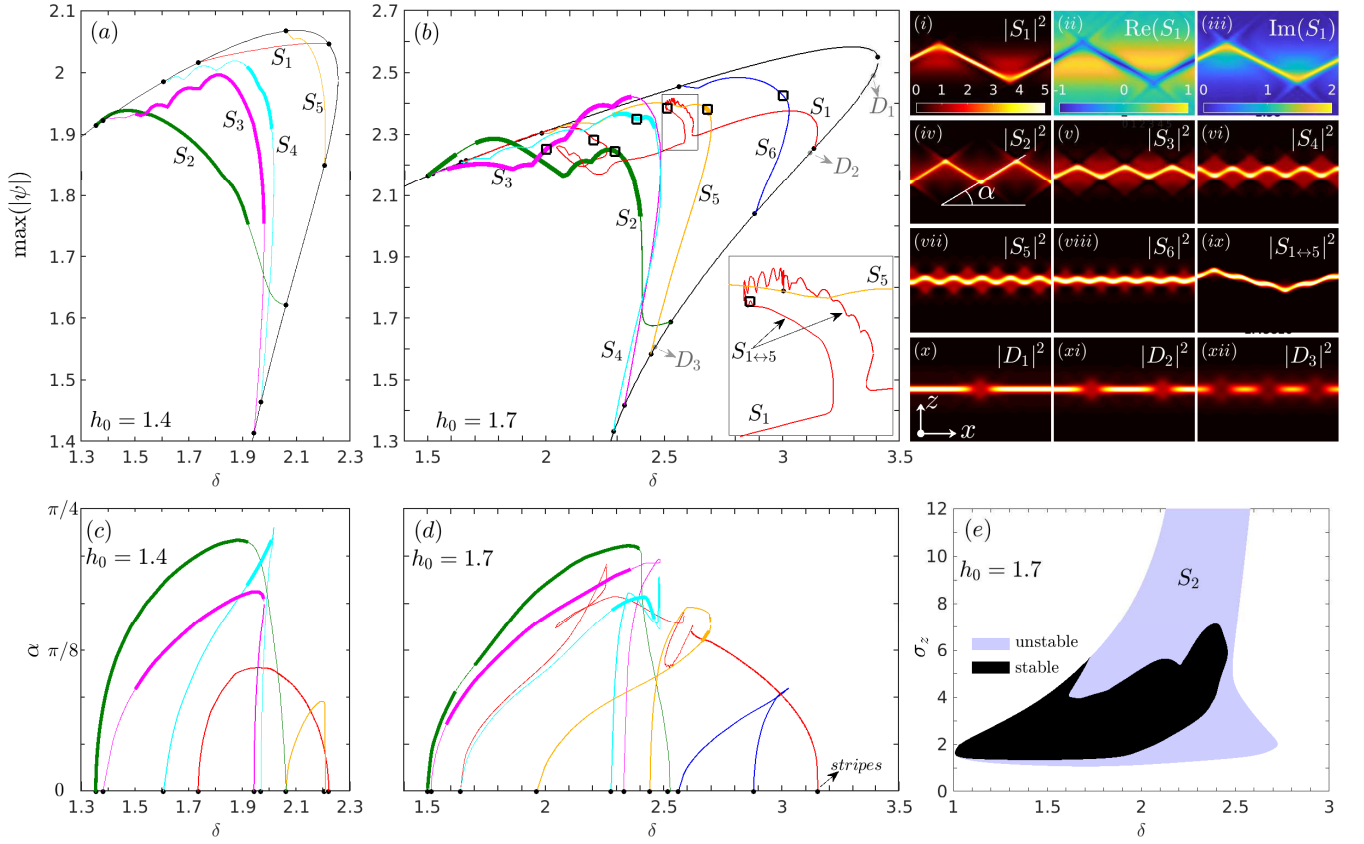


FIG. 2. | **Photonic snake families bifurcating from the single stripe background.** **a,b**, amplitude vs detuning branches for all photonic snakes supported by the microcylinder considered in Fig.1 with  $\sigma_z = 4$  for **a**  $h_0 = 1.4$  and **b**  $h_0 = 1.7$ . Thick (thin) traces denote stable (unstable) states. The nonlinear resonances (black curves) are those shown in Figs.1b and 1e, respectively. Photonic snakes exhibiting  $N$  periods around the cavity circumference are denoted by  $S_N$ , and selected profiles, at the positions of the squares in **b**, are shown in insets (i) – (viii). Panels (ii), (iii) show real, imaginary parts of the snake  $S_1$ . Inset in **b** is a zoom over the region where the  $S_1$  branch approaches the  $S_5$  branch, and as a consequence, the corresponding snakes [inset (ix)] present a profile mixing both periodicities: 5 small zigzag periods within a 1 period envelope. Other branches exist (not shown), associated to  $N$ -dark soliton states, denoted by  $D_N$ , with typical profiles as shown in (x) – (xii). **c,d** show the snake’s zigzagging angle [cf. inset (iv)] as a function of detuning,  $\alpha(\delta)$ , corresponding to all branches in **a,b** (branches are colour-matched). **e** shows the existence (light area) and stability (black area) domains in the  $\{\delta, \sigma_z\}$  plane for the snake family  $S_2$  with  $h_0 = 1.7$ . All insets are plotted over the area  $x \in [-L/2, L/2[$  and  $z \in [-8, 8]$ .

lous GVD [34] (formally analogous to diffraction along  $z$ ), the background states become single and multi-stripe solitons [cf. insets (ii)-(viii)] distributed on top of the smooth background [cf. inset (i)], recalling the spatial solitons reported in pioneering works [35]. The presence of stripes impinges an intricate morphology of the resonances strongly deviating from that of the tri-valued (bistable) one-dimensional counterparts (marked for reference by the light-grey curves in Figs.1b-g). Resonances associated to wider or more intense pumps (i.e., greater  $\sigma_z$  and  $h_0$ , respectively) contain states hosting more stripes and reshape to exhibit splitting (Figs. 1c,e), nesting (Figs. 1d,f,g), and closed loops (Fig. 1f). As discussed below, the properties of resonances are intimately linked to the existence of snake states.

**Photonic snakes.** The soliton stripes described above are prone to snake instabilities. When these develop, stripes distort and acquire in our dissipative system a

periodic zigzag snaking profile, becoming inhomogeneous along  $x$  and, hence, polychromatic. The central result of this work is that the transverse drifts induced by the snake instability are fully arrested after they exerted certain distortion to stripes so that perfectly stationary snakes form [see Figs. 2(i)-(ix) for typical profiles]. Figures 2a, b present the branches [ $\max(|\psi(x, z)|)$  vs detuning] corresponding to the complete set of snakes existing with narrow pump,  $\sigma_z = 4$ , for different driving strengths,  $h_0$  (see caption). Snakes featuring from 1 to 5 periods in the microcavity circumference exist and those with 2 to 4 periods are stable for some detuning intervals. We denote different branches of snakes featuring  $N$  periods on the microresonator circumference as  $S_N$ . Figures 2c,d show that snakes feature pronounced zigzagging angles,  $\alpha$  [cf. inset (iv)], over most of their existence regions, so that they have a strong trend to form narrow pulses along  $x$ . We emphasize that the robust snakes

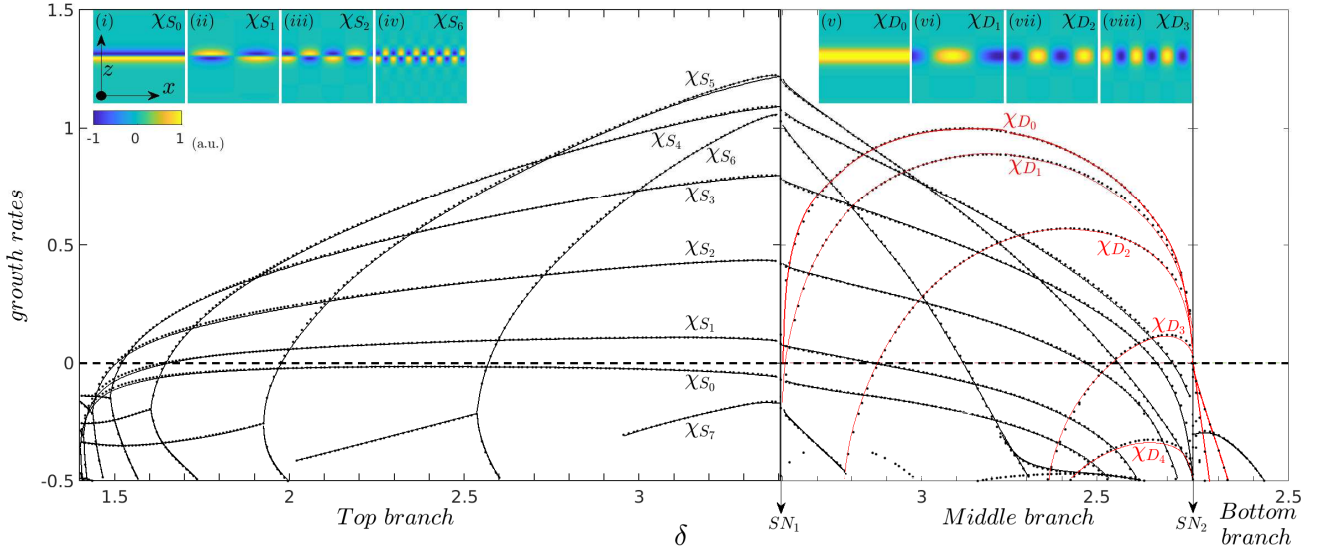


FIG. 3. | **Onset of snakes.** Growth rates vs detuning of the internal modes associated to the background states defining the cavity resonance in Fig. 1e [ $\sigma_z = 4$ ,  $h_0 = 1.7$ ]. This figure is a parametric plot along the resonance, i.e., the abscissa corresponds to the values of detuning along the branches of the resonance, starting at  $\delta = 1.4$ . The left panel ( $\delta \in [1.4, SN_1] \lesssim 3.5$ ) corresponds to the top branch, the central panel ( $\delta \in [SN_1, SN_2]$ ) corresponds to the middle branch, and the right panel ( $\delta \in [SN_2 \gtrsim 2.2, 2.5]$ ) corresponds to the lower and stable branch. Labels  $\chi_\psi$  denote the internal modes the growth of which leads to the state  $\psi$  [ $\psi$  are either snakes  $S_N$  (black) or dark solitons  $D_N$  (red)]. Insets at the top show the real part of typical snake (left) and neck (right) modes. Snake modes with  $N = 0$  induce, when excited, a global drift along  $z$  while neck modes with  $N = 0$  correspond to the *universally* unstable mode that dots the whole middle branch with the detrimental zero-wavelength instability. The zero growth rate points correspond to the bifurcation points shown in Figs. 1 and 2 from where the corresponding states (shown in Fig. 2) emerge. Insets are plotted over the area  $x \in [-L/2, L/2[$  and  $z \in [-8, 8]$ .

exist over a finite and generous region of the parameter space, as shown in Figs. 2a-d. To further illustrate this, Fig. 2e shows the existence domain on the  $\{\delta, \sigma_z\}$  plane for the  $S_2$  family, which is found to be stable within the black area, unstable within the light shaded area, and non-existent otherwise (white area). In this work, optimal conditions for the snakes stability are encountered only for strong pump localisation along  $z$ . Outside the stability domain, snakes are exposed to oscillatory and exponential instabilities leading, respectively, to breathing and decay. The precise combination of the driving amplitude and aspect ratio of the pump field,  $\sigma_z/L$ , (lying in the range  $[\frac{1}{8}, \frac{1}{3}]$  in Fig. 2e) is essential for the formation of robust snakes.

Photonic snake families emerge supercritically from the top branch of the cavity resonance, each with a different detuning threshold (marked with black dots in Fig. 2), corresponding to the detuning values at which stripes become unstable due to the growth of snake type perturbations or *internal modes* [36] (see methods for the stability analysis description). Figure 3 shows all relevant growth rates for the three branches (top, middle, and bottom) of the right-most cavity resonance shown in Fig. 1e. Snake-type perturbations ( $\chi_S$ , see top insets in Fig. 3) with different periods acquire positive growth rates on the top and middle branches of the resonance. The nullity of growth rates defines exactly the bifurcation

points (black dots in Fig. 2b) or loci from which snakes emerge from stripes. We note that the symmetry properties of the stripes internal modes allows one to readily predict the symmetries to be inherited by the emerging snake family.

Although our attention is focused on the snake instability, we point out that the middle branch of the resonance in Fig. 3 also presents *neck* instabilities [1], which often compete with the snake type [37] and manifests upon the growth of the corresponding internal modes, denoted by  $\chi_{D_1} - \chi_{D_3}$  and shown in the right inset of Fig. 3. In this work, all of the spatiotemporal states found with traces of neck perturbations, namely, the dark solitons in Figs. 2(x-iii) and the hybrid snake-dark solitons in Fig. 4j,l, were highly unstable and thus their properties are not discussed in details.

The photonic snake families become much richer when snake instabilities develop on the multi-stripe states present on cavity resonances with large pump beam widths,  $\sigma_z \gtrsim 8$  (cf. Fig. 1), what leads to the formation of coupled multi-snake states. Figure 4a shows an example of robust two-snake state with three periods along the microcylinder's circumference, denoted by  $S_3^{(2)}$ . This double snake forms when the snake-type mode  $\chi_{S_3^{(2)}}$  (Fig. 4b bottom-right inset) grows on top of the two-stripe state (Fig. 4b top-right inset). The full amplitude vs detuning branch of the  $S_3^{(2)}$  snake is shown in Fig. 4b by the



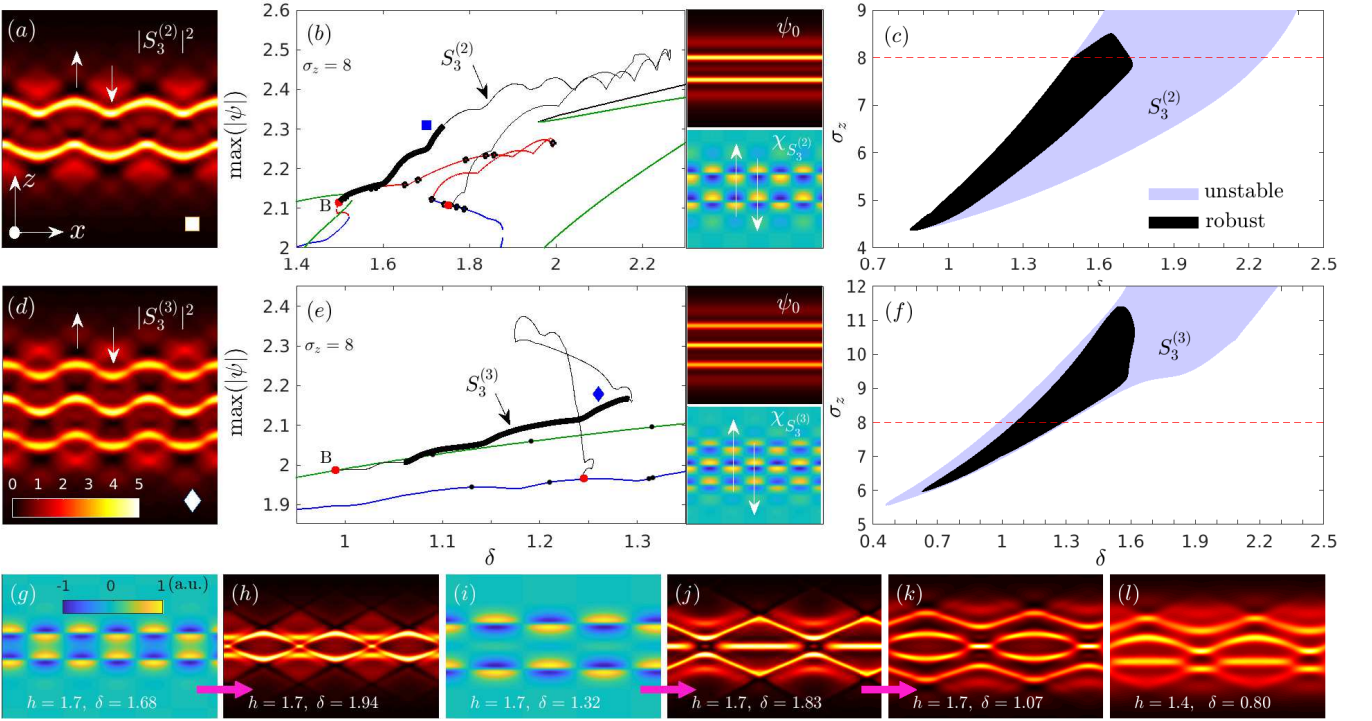


FIG. 4. **Coupled photonic snakes.** **a**, intensity of a 2-snake with 3 periods [denoted by  $S_3^{(2)}$ ] for  $h_0 = 1.7$  and  $\sigma_z = 8$ . **b**, branches of its existence and stability shown by the solid and thick black curves, respectively. Branches with other colors correspond to the resonances in Fig. 1f. A square marker is around the location where the profile in **a** is taken ( $\delta = 1.72$ ). The stable branch emerges from the bifurcation point labeled with B (left most thick red dot). Inset: (top) 2-stripe state, (bottom) perturbation impinging the flexural instability that transforms the 2-stripe state into the  $S_3^{(2)}$  in **a**. White arrows indicate the direction of the local drift [arrows in inset and in **a** are in exact correspondence]. **c**, Existence and stability chart in the  $\{\delta, \sigma_z\}$ -plane for  $h_0 = 1.7$ , built by analysing the stability of the stable branch in **b** and varying pump-width. Horizontal dashed line marks  $\sigma_z = 8$ , corresponding to **b**. **d-f** are analogous to **a-c** for a triple snake. Other snaking states, albeit unstable: **g,i** show the internal modes of the (2,3)-stripe states leading to states in **h,j**. Additional bifurcations reshape states of the type **j** into **k** and **l**. All  $(x, z)$  panels are plotted over the area  $x \in [-L/2, L/2]$  and  $z \in [-10, 10]$ .

black curve. Other branches correspond to the cavity resonance (cf. Fig. 1f). Existence and stability of the  $S_3^{(2)}$  family with  $h_0 = 1.7$  is shown vs pump width and detuning over the relevant parameter space in Fig. 4c. Figures 4d-f show analogous results for a triple-snake. The above two snake families correspond to particular cases where their branches connect background states with different number of stripes: the  $S_3^{(2)}$  [ $S_3^{(3)}$ ] family bifurcates at lower  $\delta$  from the B-point located on a 2 (3) stripe state and merges with 4-stripe state at a higher  $\delta$  (red dots).

Even though we only found stable *in-phase* multi-snakes, the system supports a vast collection of states with different morphology. Some of these are illustrated in Fig. 4h and Figs. 4j,k,l which appear after the *anti-phase* snake modes in Figs. 4g and 4i grow, respectively, on two- and three-stripe states. This results in the formation of anti-phase snakes that appear alone (Fig. 4h), mixed with dark solitons (Fig. 4j), together with ellipsoids (Fig. 4k), or displaying asymmetries along  $z$  (Fig. 4l).

**Heterogeneous 2D combs.** The most remarkable fea-

ture of photonic snake states is that their spectrum is heterogeneous along  $z$ , while being inherently synchronized by the nonlinearity. Figure 5 shows a soliton stripe (Fig. 5a) and snakes of different tilts and periods (Figs. 5b-d), together with their frequency comb distribution along  $z$  (Figs. 5e-h). Heterogeneity is evident in Figs. 5g,h, showing Fourier spectra along the  $z$ -axis, and it is further illustrated in insets I – IV by showing different combs extracted at different axial positions (marked by horizontal white lines in Figs. 5c,g). Synchronisation and heterogeneity of these spectra is readily important for metrology and spectroscopy [38]. The spreading of the combs along the cylinder's axis,  $z$ , naturally introduces the notion of heterogeneous two-dimensional comb, which constitutes a generalisation of the widely reported one-dimensional comb and a central result of this work.

Figures 5i-l show the snakes in Figs. 5a-d, respectively, in the two-dimensional momentum space, illustrating the angular spread of the different spectral components, potentially important for an efficient collection of the combs by external tapers or waveguides. Because dispersion in cylinders is typically much smaller in  $x$  than in  $z$  [39, 40],

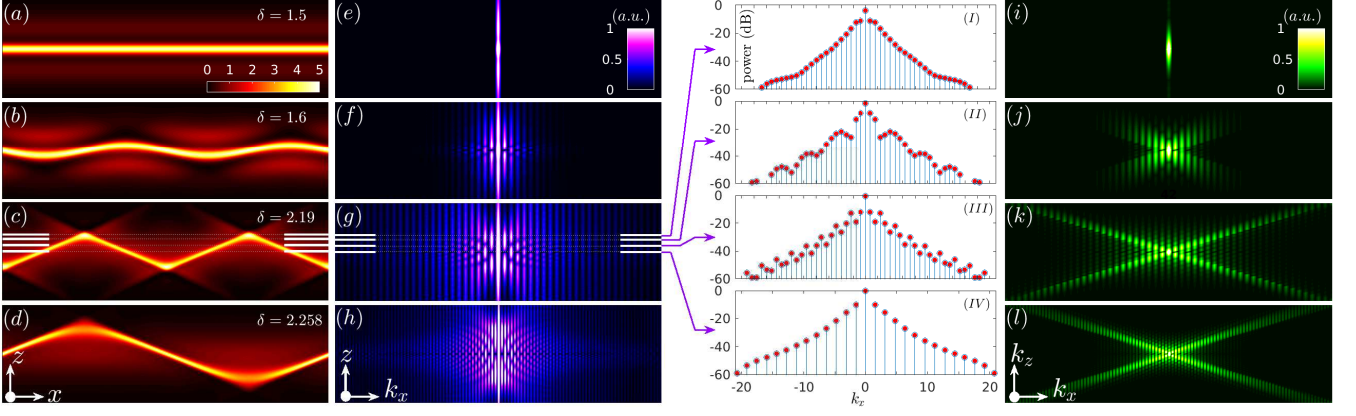


FIG. 5. **Two-dimensional heterogeneous combs.** **a-d**, intensity,  $|\psi(x, z)|^2$ , for several snake profiles with different tilt,  $\alpha$ , periodicity, and detuning,  $\delta$  (see labels) at  $\sigma_z = 4$  and  $h_0 = 1.7$ . **e-h**, Fourier transform along the  $x$  direction of the fields in **a-d**, illustrating the two-dimensional comb structure vs  $z$  around the central wave-numbers,  $k_x$ . The frequency combs exhibit a high degree of heterogeneity along the cylinder's axis ( $z$ ), as evident from insets (I)-(IV), showing the broad one-dimensional combs at different locations:  $z = 1.72, 1.25, 0.63, 0$ , respectively. **i-l**, Two-dimensional Fourier transforms of the fields in **a-d** illustrating snakes in momentum space, which reveal the angular spread of the two-dimensional comb frequencies (see text). Figure axes: **a-d**,  $x \in [-L/2, L/2]$  and  $z \in [-5, 5]$ ; **e-h**,  $k_x \in [-20, 20]$  and  $z \in [-5, 5]$ ; **i-l**,  $k_x \in [-20, 20]$  and  $k_z \in [-20, 20]$ . Spectra in **e-l** are normalised to the strongest comb line excluding the pump at  $k_x = 0$ .

the physical values corresponding to  $k_z$  are in practice much smaller than those corresponding to  $k_x$ , so that the propagation angles  $\theta = \arctan(k_z/k_x)$  remain in the order of a few degrees, at most (see methods). On the same reason, the height of panels  $e - h$  is of the order of a few mm's, so that the comb heterogeneity occurs along  $z$  over larger scale than typical taper fiber widths, which enables the efficient light collection by, e.g., arrays of waveguides.

**Robustness.** The photonic snakes and the two-dimensional combs exist in a physical setting that is readily realizable. In particular, consider a hollow micro-cylinder made of silica glass, with a radius  $R = 100 \mu\text{m}$  and wall thickness  $w = 0.75 \mu\text{m}$ , pumped at  $\lambda_p \approx 1.26 \mu\text{m}$ , with a  $Q$ -factor of  $\sim 5 \times 10^6$ , and take into account the expected specific effects introduced by chromatic dispersion, Raman and thermal nonlinearities, and the localised coupling, in  $x$  and  $z$ , between the pump beam and the micro-cavity (see the full model in methods). Although each of the above *perturbations* may be suppressed in various ways, we now show that robust snakes occur in passive driven cylindrical micro-resonators. Figure 6 presents an overview of our predictions in such scenarios, focusing the attention on the snake family  $S_2$  with  $h_0 = 1.4$  and  $\sigma_z = 4$ . Figure 6a shows the thermal shift of the nonlinear resonance [black] with respect to the unperturbed cold resonance [grey], as well as the  $S_2$  snake branch, which stable region is highlighted by the thick trace. An example of robust snake is shown in Fig.6b, along with its associated Raman vibration (Fig.6c) and thermal (Fig.6d) fields. The corresponding two-dimensional comb is shown around the central lines in Fig.6e. We emphasize that in the context of one-dimensional combs, solitons and related nonlin-

ear waves have been reported under the thermal non-linearity [41], both experimentally [21] and theoretically [42]. In one dimension, thermal effects mainly induce a global shift in the laser-cavity detuning which, even if they introduce their own instabilities [41, 42], cannot compromise soliton existence itself. However, in the two-dimensional case here considered, thermal effects are inhomogeneous along  $z$  (cf. Fig.6d), and hence induce *thermal stress* along  $z$ . As a consequence, the mere existence of the two-dimensional snakes cannot be anticipated *a priori*, and neither can their stability. The latter is formally predicted via linear stability analysis and explicitly checked by long propagation runs (cf. Fig.6f) spanning over 50,000 cavity roundtrips (equivalent to 155 ns in our geometry). Propagation of robust snakes under the whole plethora of realistic effects feature constant peak amplitudes (as a consequence of the steady two-dimensional profiles) despite the input random noise and step-to-step perturbations. On the contrary, unstable snakes behave very differently. In particular, Fig.6g shows the time evolution of an oscillatory unstable snake, featuring peak amplitude and profile variations (see insets). The presence and absence of instabilities, and the nature of them in the former case, are accurately predicted by the stability analysis (see methods), which results are displayed in insets of Figs.6f,g.

## Discussion.

Stable photonic snakes present a trend to bifurcate super-critically from the stable background upon the increase of detuning [cf. Figs. 2,4], even in the presence of *higher order effects* [cf. Fig. 6], what strongly suggests that they will be easily and deterministically excitable in realistic experiments by the standard dynamical red-shift of the pump's frequency. This simple excitation mechanism

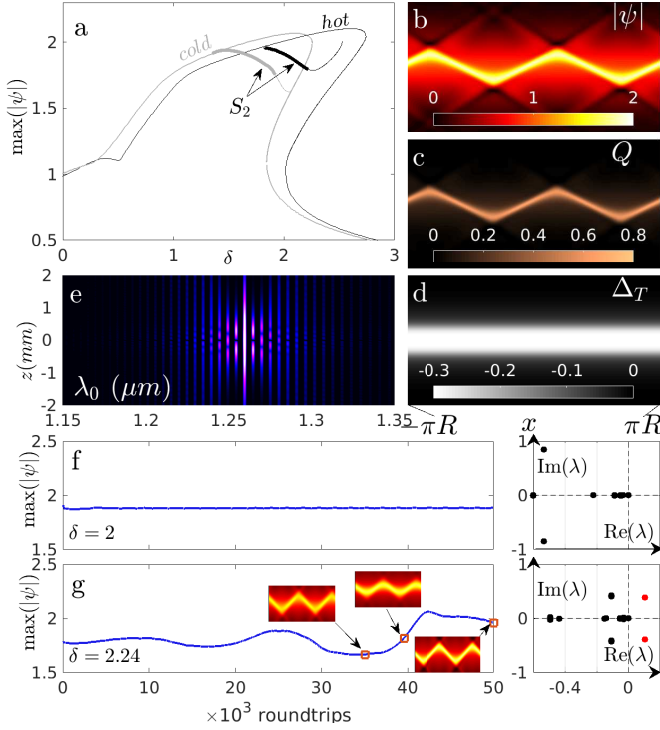


FIG. 6. **Effect of perturbations.** **a**, cavity resonance and the branch for the two-period snakes,  $S_2$ , affected by perturbation originating from higher order dispersion, Raman scattering and thermal nonlinearity (black) [resonance is solely affected by thermal effects, and hence the label *hot*]. The results without perturbations are also shown for reference (gray, cf. Fig.2a). **b-d** show, respectively, the light field, the Raman vibration, and the thermal distribution for the stable snake at  $\delta = 2$ . **e**, the corresponding two-dimensional comb. **f**, the maximum amplitude of the light field during the propagation of the stable and robust snake ( $\delta = 2$ ), for a total time of 155 ns [50,000 roundtrips], under initial noise and perturbations at each step. Right-inset: complex eigenvalues,  $\lambda$ , obtained from the stability analysis performed on the stationary snake used as input of the propagation, taking into account all above mentioned perturbations. Instabilities correspond to positive real parts of  $\lambda$ . **g**, analogous results as for **f**, but for an oscillatory unstable snake ( $\delta = 2.24$ ). Small insets illustrate the dynamical reshaping of the snake with time. Panels **b-d** and insets in **g** span over the whole cavity circumference and over 4 mm along  $z$ .

of frequency combs in the normal GVD regime of passively driven cavities, naturally provided here by the intrinsically two-dimensional snakes, has remained hidden till date by the low dimensionality of microrings, where relatively complex excitation methods were typically required. Indeed, in one-dimensional microrings, solitonic combs in the normal GVD regime are often excited by engineering a small anomalous GVD region around the

pump's frequency, so modulational instability triggers comb formation. This is achieved via mode coupling effects arising due to avoided crossings in multi-modal microrings [43–46] or with the aid of an auxiliary ring [47, 48]. A recent work demonstrates a much simpler and straight-forward mechanism to excite (one-dimensional) dark solitons via self-injection-locking [49] and displaying the turnkey [50] operation. Photonic snake states may thus belong to the collection of simple and deterministically excitable combs in cavities with dominant normal GVD, which is of central importance for extending the formation of micro-cavity combs to the long and short wavelength regions, far away from the telecom band around  $1.5 \mu\text{m}$ .

In addition, the two-dimensional combs reported here automatically enable the possibility to host synchronised heterogeneous combs in a single device, features that are of great importance in metrology and spectroscopy, and may be difficult to combine in this specific manner with microrings. Indeed, comb heterogeneity may be achieved in the one-dimensional context, e.g., via the excitation of unbounded solitons copropagating along the same spatial channel [51]. However, their different group velocities unavoidably yield de-synchronisation. On the other hand, synchronisation was previously reported for identical combs in distant microrings [52]. Remarkably, both features were found simultaneously in the bi-modal stokes solitons [19], where heterogeneity appeared as a result of two copropagating and spectrally non-overlapping combs. In the present work, differently with the above, and akin to the two-dimensional geometry, the heterogeneity appears as a continuous comb reshaping along the cylinder's axis and with a fixed carrier frequency. We note that the above remarkable findings [19, 51, 52] were reported in the anomalous GVD region, where the physics is substantially different than that in the normal GVD regime, subject of this work.

In summary, we have uncovered a fundamentally new mechanism to arrest and control the ubiquitous and otherwise strong snake instability in cylindrical Kerr microresonators and, as a result, the possibility to form complex robust spatiotemporal snake states. Specifically, we have found that photonic snakes naturally form perfectly synchronised heterogeneous comb ensembles in the normal GVD (hyperbolic) regime of cylindrical microcavities. The phenomenon represents a novel paradigm for the generation of optical frequency combs.

## Online content

Methods, additional references, statements of data availability, acknowledgements, details of author contributions and competing interests are available in the online version of the paper.

[1] V. E. Zakharov, A. M. Rubenchik, “Instability of waveguides and solitons in nonlinear media,” Sov. Phys. JETP



- [2] E. A. Kuznetsov, A. M. Rubenchik, V. E. Zakharov, "Soliton stability in plasmas and hydrodynamics," *Phys. Rep.* **142**, 103–65 (1986).
- [3] Y. S. Kivshar and D. E. Pelinovsky, "Self-focusing and transverse instabilities of solitary waves," *Phys. Rep.* **331**, 117–195 (2000).
- [4] J. A. Constantin, T. Dunne, J. Ahmed, C. Legleiter, and E. D. Lazarus, "Sediment supply as a driver of river meandering and floodplain evolution in the Amazon Basin," *Nature Geoscience* **7**, 899–903 (2014).
- [5] E. D. Brown, S. B. Buchsbaum, R. E. Hall, J. P. Penhune, K. F. Schmitt, K. M. Watson, and D. C. Wyatt, "Observations of a nonlinear solitary wave packet in the Kelvin wake of a ship," *J. Fluid Mech.* **204**, 263–293 (1989).
- [6] T. Yefsah, A. T. Sommer, M. J. Ku, L. W. Cheuk, W. Ji, W. S. Bakr, and M. W. Zwierlein, "Heavy solitons in a fermionic superfluid," *Nature* **499**, 426–430 (2013).
- [7] A. Cetoli, J. Brand, R. G. Scott, F. Dalfovo, and L. P. Pitaevskii, "Snake instability of dark solitons in fermionic superfluids," *Phys. Rev. A* **88**, 043639 (2013).
- [8] F. Claude, S. V. Koniakhin, A. Maitre, S. Pigeon, G. Lerrario, D. D. Stupin, Q. Glorieux, E. Giacobino, D. Solnyshkov, G. Malpuech, and A. Bramati, "Taming the snake instabilities in a polariton superfluid," *Optica* **7**, 1660–1665 (2020).
- [9] B. P. Anderson, P. C. Haljan, C. A. Regal, D. L. Feder, L. A. Collins, C. W. Clark, and E. A. Cornell, "Watching dark solitons decay into vortex rings in a Bose-Einstein condensate," *Phys. Rev. Lett.* **86**, 2926–2929 (2001).
- [10] C. Luengviriya, U. Storb, G. Lindner, S. C. Müller, M. Bär, and M. J. B. Hauser, "Scroll Wave Instabilities in an Excitable Chemical Medium," *Phys. Rev. Lett.* **100**, 148302 (2008).
- [11] A. V. Mamaev, M. Saffman, and A. A. Zozulya, "Propagation of dark stripe beams in nonlinear media: snake instability and creation of optical vortices," *Phys. Rev. Lett.* **76**, 2262–2265 (1996).
- [12] V. Tikhonenko, J. Christou, B. Luther-Davies, and Y. S. Kivshar, "Observation of vortex solitons created by the instability of dark soliton stripes," *Opt. Lett.* **21**, 1129–1131 (1996).
- [13] S.-P. Gorza, N. Roig, Ph. Emplit, and M. Haelterman, "Snake Instability of a Spatiotemporal Bright Soliton Stripe," *Phys. Rev. Lett.* **92**, 084101 (2004).
- [14] S.-P. Gorza, Ph. Emplit, and M. Haelterman, "Observation of the snake instability of a spatially extended temporal bright soliton," *Opt. Lett.* **31**, 1280–1282 (2006).
- [15] S.-P. Gorza, B. Deconinck, Ph. Emplit, T. Trogdon, and M. Haelterman, "Experimental Demonstration of the Oscillatory Snake Instability of the Bright Soliton of the  $(2 + 1)D$  Hyperbolic Nonlinear Schrödinger Equation," *Phys. Rev. Lett.* **106**, 094101 (2011).
- [16] V. Brasch, M. Geiselmann, T. Herr, G. Lihachev, M. H. P. Pfeiffer, M. L. Gorodetsky, and T. J. Kippenberg, "Photonic chip-based optical frequency comb using soliton Cherenkov radiation," *Science* **351**, 357–360 (2016).
- [17] X. Yi, Q.-F. Yang, X. Zhang, K. Y. Yang, X. Li, and K. Vahala, "Single-mode dispersive waves and soliton microcomb dynamics," *Nat. Commun.* **8**, 1–9 (2017).
- [18] M. Karpov, H. Guo, A. Kordts, V. Brasch, M. H. P. Pfeiffer, M. Zervas, M. Geiselmann, and T. J. Kippenberg, "Raman self-frequency shift of dissipative Kerr solitons in an optical microresonator," *Phys. Rev. Lett.* **116**, 103902 (2016).
- [19] Q.-F. Yang, X. Yi, K. Y. Yang, and K. Vahala, "Stokes solitons in optical microcavities," *Nat. Phys.* **13**, 53–57 (2017).
- [20] M. Yu, Y. Okawachi, R. Cheng, C. Wang, M. Zhang, A. L. Gaeta, and M. Lončar, "Raman lasing and soliton mode-locking in lithium niobate microresonators," *Light: Science & Applications* **9**, 1–7 (2020).
- [21] J. R. Stone, T. C. Briles, T. E. Drake, D. T. Spencer, D. R. Carlson, S. A. Diddams, and S. B. Papp, "Thermal and nonlinear dissipative-soliton dynamics in Kerr-microresonator frequency combs," *Phys. Rev. Lett.* **121**, 063902 (2018).
- [22] E. Obrzud, S. Lacomte, and T. Herr, "Temporal solitons in microresonators driven by optical pulses," *Nat. Photon.* **11**, 600–607 (2017).
- [23] A. Pasquazi, M. Peccianti, L. Razzari, D. J. Moss, S. Coen, M. Erkintalo, Y. K. Chembo, T. Hansson, S. Wabnitz, P. Del'Haye, X. Xue, A. M. Weiner, and R. Morandotti, "Micro-combs: a novel generation of optical sources," *Phys. Rep.* **729**, 1–81 (2017).
- [24] S. T. Cundiff and J. Ye, "Colloquium: Femtosecond optical frequency combs," *Rev. Mod. Phys.* **75**, 325–342 (2003).
- [25] Q. F. Yang, X. Yi, K. Y. Yang, and K. Vahala, "Counter-propagating solitons in microresonators," *Nat. Photon.* **11**, 560–564 (2017).
- [26] W. Weng, R. Bouchand, E. Lucas, and T. J. Kippenberg, "Polychromatic Cherenkov radiation induced group velocity symmetry breaking in counterpropagating dissipative Kerr solitons," *Phys. Rev. Lett.* **123**, 253902 (2019).
- [27] A. Tikan, J. Riemensberger, K. Komagata, S. Hönl, M. Churav, C. Skehan, H. Guo, R. N. Wang, J. Liu, P. Seidler, and T. J. Kippenberg, "Emergent nonlinear phenomena in a driven dissipative photonic dimer," *Nat. Phys.* **17**, 604–610 (2021).
- [28] J. K. Jang, X. Ji, C. Joshi, Y. Okawachi, M. Lipson, and A. L. Gaeta, "Observation of Arnold Tongues in Coupled Soliton Kerr Frequency Combs," *Phys. Rev. Lett.* **123**, 153901 (2019).
- [29] E. Lucas, G. Lihachev, R. Bouchand, N. G. Pavlov, A. S. Raja, M. Karpov, M. L. Gorodetsky, and T. J. Kippenberg, "Spatial multiplexing of soliton microcombs," *Nat. Photon.* **12**, 699–705 (2018).
- [30] L. A. Lugiato and R. Lefever, "Spatial dissipative structures in passive optical systems," *Phys. Rev. Lett.* **58**, 2209–2211 (1987).
- [31] C. Conti, S. Trillo, P. Di Trapani, G. Valiulis, A. Piskarskas, O. Jedrkiewicz, and J. Trull, "Nonlinear electromagnetic X waves," *Phys. Rev. Lett.* **90**, 170406 (2003).
- [32] P. Di Trapani, G. Valiulis, A. Piskarskas, O. Jedrkiewicz, J. Trull, C. Conti, and S. Trillo, "Spontaneously generated X-shaped light bullets," *Phys. Rev. Lett.* **91**, 093904 (2003).
- [33] L. A. Cisneros-Ake, R. Carretero-González, P. B. Kevrekidis, and B. A. Malomed, "Dynamics and stabilization of bright soliton stripes in the hyperbolic-dispersion nonlinear Schrödinger equation," *Commun. Nonlinear Sci. Numer. Simul.* **74**, 268–281 (2019).
- [34] I. Barashenkov and Y. S. Smirnov, "Existence and stability chart for the ac-driven, damped nonlinear Schrödinger solitons," *Phys. Rev. E* **54**, 5707–5725 (1996).
- [35] D. W. Mc Laughlin, J. V. Moloney, and A. C. Newell, "Solitary Waves as Fixed Points of Infinite-Dimensional Maps in an Optical Bistable Ring Cavity," *Phys. Rev.*



- Lett. **51**, 75–78 (1983).
- [36] D. E. Pelinovsky, Y. S. Kivshar, and V. V. Afanasjev, “Internal modes of envelope solitons,” *Physica D* **116**, 121–142 (1998).
  - [37] D. V. Skryabin and W. J. Firth, “Modulational instability of solitary waves in non-degenerate three wave mixing: the role of phase symmetries,” *Phys. Rev. Lett.* **81**, 3379–3382 (1998).
  - [38] N. Picqué and T. W. Hänsch, “Frequency comb spectroscopy,” *Nat. Photon.* **13**, 146–157 (2019).
  - [39] Y. A. Demchenko and M. L. Gorodetsky, “Analytical estimates of eigenfrequencies, dispersion, and field distribution in whispering gallery resonators,” *J. Opt. Soc. Am. B* **30**, 3056–3063 (2013).
  - [40] C. Milián, Y. V. Kartashov, D. V. Skryabin, and L. Torner, “Clusters of cavity solitons bounded by conical radiation,” *Phys. Rev. Lett.* **121**, 103903 (2018).
  - [41] V. S. Ilchenko and M. L. Gorodetskii, “Thermal nonlinear effects in optical whispering gallery microresonators,” *Laser Phys.* **2**, 1004–1009 (1992).
  - [42] A. Leshem, Z. Qi, T. F. Carruthers, C. R. Menyuk, and O. Gat, “Thermal instabilities, frequency-comb formation, and temporal oscillations in Kerr microresonators,” *Phys. Rev. A* **103**, 013512 (2021).
  - [43] A. A. Savchenkov, A. B. Matsko, W. Liang, V. S. Ilchenko, D. Seidel, and L. Maleki, “Kerr frequency comb generation in overmoded resonators,” *Opt. Express* **20**, 27290–27298 (2012).
  - [44] X. Xue, Y. Xuan, Y. Liu, P.-H. Wang, S. Chen, J. Wang, D. E. Leaird, M. Qi, and A. M. Weiner, “Mode-locked dark pulse Kerr combs in normal-dispersion microresonators,” *Nat. Photon.* **9**, 594–600 (2015).
  - [45] J. K. Jang, Y. Okawachi, M. Yu, K. Luke, X. Ji, M. Lipson, and A. L. Gaeta, “Dynamics of mode-coupling-induced microresonator frequency combs in normal dispersion,” *Opt. Express* **24**, 28794–28803 (2016).
  - [46] E. Nazemosadat, A. Fülöp, Ó. B. Helgason, P.-H. Wang, Y. Xuan, D. E. Leaird, M. Qi, E. Silvestre, A. M. Weiner, and V. Torres-Company, “Switching dynamics of dark-pulse Kerr frequency comb states in optical microresonators,” *Phys. Rev. A* **103**, 013513 (2021).
  - [47] X. Xue, Y. Xuan, P.-H. Wang, Y. Liu, D. E. Leaird, M. Qi, and A. M. Weiner, “Normal-dispersion microcombs enabled by controllable mode interactions,” *Laser Photon. Rev.* **9**, L23–L28 (2015).
  - [48] B. Y. Kim, Y. Okawachi, J. K. Jang, M. Yu, X. Ji, Y. Zhao, C. Joshi, M. Lipson, and A. L. Gaeta, “Turnkey, high-efficiency Kerr comb source,” *Opt. Lett.* **44**, 4475–4478 (2019).
  - [49] W. Jin, Q.-F. Yang, L. Chang, B. Shen, H. Wang, M. A. Leal, L. Wu, M. Gao, A. Feshali, M. Paniccia, K. J. Vahala, J. E. Bowers, “Hertz-linewidth semiconductor lasers using CMOS-ready ultra-high-Q microresonators,” *Nat. Photon.* **15**, 346–353 (2021).
  - [50] B. Shen, L. Chang, J. Liu, H. Wang, Q. F. Yang, C. Xiang, R. N. Wang, J. He, T. Liu, W. Xie, J. Guo, D. Kinghorn, L. Wu, Q. Ji, T. J. Kippenberg, K. Vahala, and J. E. Bowers, “Integrated turnkey soliton microcombs,” *Nature* **582**, 365–369 (2020).
  - [51] W. Weng, R. Bouchand, E. Lucas, E. Obrzud, T. Herr, and T. J. Kippenberg, “Heteronuclear soliton molecules in optical microresonators,” *Nat. Commun.* **11**, 1–9 (2020).
  - [52] J. K. Jang, A. Klenner, X. Ji, Y. Okawachi, M. Lipson, and A. L. Gaeta, “Synchronization of coupled optical microresonators,” *Nat. Photon.* **12**, 688–693 (2018).

## Online Methods

**Time evolution equations.** The nonlinear dynamics of the electric field's envelope orbiting around a cylindrical microresonator is described by the following system of coupled equations,

$$i\partial_t\psi = -ib_{1,1}\partial_X\psi + \frac{1}{2}(\partial_X^2 - \partial_z^2)\psi + \hat{D}_{hod}\psi - [i - \delta]\psi - [(1 - f_R)|\psi|^2 - \Delta_T + Q]\psi - h_0 \exp\left(-\frac{z^2}{\sigma_z^2}\right)\xi(X), \quad (2)$$

$$\partial_t\Delta_T = -A \int_0^L |\psi|^2 \frac{dX}{L} - B\Delta_T, \quad (3)$$

$$\partial_t^2 Q = -\frac{2\gamma_R\tau}{\gamma}\partial_t Q - \frac{\tau^2\Omega_R^2}{\gamma^2}[Q - f_R|\psi|^2], \quad (4)$$

$$\xi(X) = \frac{1}{N} \sum_{m=-\infty}^{+\infty} \exp\left(-\frac{[X + mL]^2}{\sigma_X^2}\right), \quad (5)$$

where  $\psi$ ,  $\Delta_T$ ,  $Q$  are the optical, thermal, and molecular vibrational fields, respectively. The above model assumes that only one radial mode family of the cylinder is at play, which may be unambiguously achieved by considering a hollow cylinder with an thin wall width, e.g.,  $w = 0.75 \mu\text{m}$ , as we used in Fig.6. The cylinder's dispersion is given by

$$\hat{D} \equiv \sum_{q=0}^{+\infty} \sum_{p=q}^{+\infty} b_{q,p-q} (-i\partial_z)^{p-q} (-i\partial_X)^q, \quad (6)$$

$$b_{q,p-q} \equiv \frac{B_{q,p-q}\gamma^{p/2-1}}{2^{p/2}|B_{0,2}|^{(p-q)/2}|B_{2,0}|^{q/2}}, \quad (7)$$

$$B_{q,p-q} \equiv \frac{\tau\omega^{(q,p-q)}}{q!(p-q)!(2\pi R)^p}, \quad (8)$$

$$\omega^{(q,p-q)} \equiv \partial_{k_x}^q \partial_{k_z}^{p-q} \omega(k_x, k_z)|_{k_{x0}, k_{z0}}, \quad (9)$$

where  $\gamma$  is the normalised cavity loss,  $R$  is the cylinder's radius,  $\tau$  the roundtrip time, and  $k_x, k_z$  the wavenumbers associated to the  $X, z$  coordinates ( $X$  is the frame at rest in the lab). The dispersion terms with low  $p, q$  indices account for:  $p = 0, q = 0$ , resonance frequency ( $\omega_0$ );  $p = 1, q = 1$ , group velocity of the pump's frequency along  $X$  ( $b_{1,1}$ );  $p = 2, q = 2$ , GVD;  $p = 2, q = 0$ , diffraction. The rest of terms are all included in the *higher order dispersion* operator  $\hat{D}_{hod} \equiv \hat{D} - \omega_0\tau/\gamma + ib_{1,1}\partial_X - \frac{1}{2}(\partial_X^2 - \partial_z^2)$ . The even parity of the cylinder's dispersion around  $z$  (see, e.g., [1, 2]) and the fact that we expand around the  $k_{z0} = 0$  yields the nullity of all coefficients with  $p - q = 1$ . The relation between normalised and physical coordinates is as follows:  $X = X_{phys}/(2\pi R)\sqrt{\gamma/(2|B_{2,0}|)}$ ,  $z = Z_{phys}/(2\pi R)\sqrt{\gamma/(2|B_{0,2}|)}$ .

In our simulations, the width of the numerical window along  $x$  was  $L = 16$ , which together with the choice of  $\gamma = 0.001$  sets  $B_{2,0} \approx -2 \times 10^{-6}$ , attainable with a silica glass cylinder of  $R = 100 \mu\text{m}$  and wall-width  $w = 0.75 \mu\text{m}$  at  $\lambda_p \approx 1.26 \mu\text{m}$ , which features a roundtrip time

$\tau = 3.1 \text{ ps}$  and a quality factor  $\mathcal{Q} = \omega_p\tau/\gamma \approx 4.9 \times 10^6$  ( $\omega_p = 2\pi c/\lambda_p$ ), reasonable for cylinders [3]. The main higher dispersion terms are given by  $B_{3,0} \approx 9.26 \times 10^{-10}$ ,  $B_{4,0} \approx -2.83 \times 10^{-13}$ ,  $B_{0,2} \approx 1.21 \times 10^{-4}$ . The normalised detuning is  $\delta = (\omega_p - \omega_0)\tau/\gamma$ .

The pump beam, assumed of Gaussian profile, has an amplitude  $h_0$  and a width  $\sigma_z$ . Under realistic conditions (cf. Fig.6), the pump beam is also localised along  $X$ , and this is accounted for via the function  $\xi(X)$ , where  $N$  is the normalisation factor such that  $\max(\xi(X)) = 1$ .

Thermal effects are introduced via the light-to-phonon energy conversion,  $A = 10^{-2}$ , and the corresponding cooling rate,  $B = 5 \times 10^{-2}$ , considering realistic values [4]. Thermal detuning,  $\Delta_T$ , is assumed not to depend on  $X$  since  $\tau \sim \text{ps}$  is much smaller than the temperature diffusion time scale, in the order of the ns. Last, we note that in Eq.3 we omitted a term  $\sim \mu\partial_z\Delta_T$ , accounting for the heat diffusion along  $z$ , as its relative importance to the other terms is of the order of  $\sim 10^{-6}$  (the thermal diffusion coefficient is  $\mu \approx 7.25 \times 10^{-7} \text{ m}^2/\text{s}$  [5]).

Raman scattering is introduced via the molecular vibrational field [6], previously implemented in microresonators [7], with standard parameter for glass given by [8]: Raman to Kerr effective fraction,  $f_R = 0.18$ ; inverse phonon life-time,  $\gamma_R = 1/32 \text{ fs}^{-1}$ ; natural phonon frequency,  $\omega_R = 1/12.2 \text{ fs}^{-1}$ ; and  $\Omega_r \equiv [\gamma_R^2 + \omega_R^2]^{1/2}$ .

Eq.1 in the main text is a particular case of the system Eqns.2-4 when higher order dispersion, Raman scattering, thermal detuning, and pump azimuthal's localisation are disregarded ( $\hat{D}_{hod} = Q = \Delta_T = 0$ ,  $\xi(X) = 1$ ). The time evolution of the above system, Eqns.2-5, is simulated via the fourth order Runge-Kutta method.

**Computation of stationary snakes.** Stationary solutions (snakes or else) are obtained numerically from Eq.1 or Eqns. 2-5 with the Newton-Raphson method in the frame comoving with the nonlinear state, where they readily satisfy  $\partial_t\psi = 0$ . While equation 1 is already expressed in such frame, Eqns.2-5 (expressed in the lab frame) are rewritten into the comoving frame after the substitution  $x = X - (b_{1,1} + v)t$ , where  $v$  is a velocity shift induced by the higher order effects, which is computed together with the nonlinear solution. When computing stationary states, the  $x$ -localisation of the pump is disregarded (we set  $\xi(X) = 1$ ).

**Stability of snakes.** Linear stability analysis is performed to all stationary solutions, represented by the tuple  $\{\psi_s Q_s, \Delta_{T_s}\}$ . Each field in the stationary solution is prone to develop instabilities. In the initial stages of such instabilities fields are regarded as  $\psi = \psi_s + ae^{i\lambda t} + b^*e^{-i\lambda^*t}$ ,  $Q = Q_s + ce^{i\lambda t} + c^*e^{-i\lambda^*t}$ ,  $\Delta_T = \Delta_{T_s} + de^{i\lambda t} + d^*e^{-i\lambda^*t}$  (Note  $Q, \Delta_T$  are real fields), where  $\lambda$  are the complex eigenvalues of the Jacobian matrix, obtained after substitution of the above decomposition into the system of Eqns. 2-4 (with  $\xi(X) = 1$ ) and linearising in  $\lambda$ . The real parts of  $\lambda$ ,  $\text{Re}(\lambda)$ , are the growth rates yielding instabilities when  $\text{Re}(\lambda) > 0$ .

### Data availability

The data that support the plots within this paper and other findings of this study are available from the corresponding author upon reasonable request.

### Code availability

The analysis codes will be made available on reasonable request.

### Acknowledgements

JAC and CM acknowledge support from the Spanish government via the Grant PID2021-124618NB-C21 funded by MCIN/AEI/ 10.13039/501100011033 and by “ERDF A way of making Europe”, by the “European Union”. CM acknowledges support from Generalitat Valenciana PROMETEO/2021/082. PFC acknowledges partial support from the Spanish

gouvernement via the project PID2021-128676OB-I00 (MICINN). LT acknowledges support by CEX2019-000910-S [MCIN/AEI/10.13039/501100011033], Fundació Cellex, Fundació Mir Puig, and Generalitat de Catalunya (CERCA). YVK academic research has been supported by the research project FFUU-2021-0003 of the Institute of Spectroscopy of the Russian Academy of Sciences.

### Author contributions

SBI and CM carried out the numerical simulations. CM conceived the project. All authors contributed significantly to this work, discussed the results, and contributed into the manuscript preparation.

### Competing interests

The authors declare no competing interests.

- 
- [1] Y. A. Demchenko and M. L. Gorodetsky, “Analytical estimates of eigenfrequencies, dispersion, and field distribution in whispering gallery resonators,” *J. Opt. Soc. Am. B* **30**, 3056–3063 (2013).
  - [2] M. Ibanescu, S. G. Johnson, D. Roundy, C. Luo, Y. Fink, and J. D. Joannopoulos, “Anomalous Dispersion Relations by Symmetry Breaking in Axially Uniform Waveguides,” *Phys. Rev. Lett.* **92**, 063903 (2004).
  - [3] M. Sumetsky, “Mode localization and the Q-factor of a cylindrical microresonator,” *Opt. Lett.* **35**, 2385–2387 (2010).
  - [4] A. Leshem, Z. Qi, T. F. Carruthers, C. R. Menyuk, and O. Gat, “Thermal instabilities, frequency-comb formation, and temporal oscillations in Kerr microresonators,” *Phys. Rev. A* **103**, 013512 (2021).
  - [5] T. Katsura, “Thermal Diffusivity of Silica Glass at Pressures up to 9 GPa,” *Phys. Chem. Min.* **20**, 201–208 (1993).
  - [6] R. Boyd, “Nonlinear Optics” (Academic Press, New York, 2008).
  - [7] C. Milián, A. V. Gorbach, M. Taki, A. V. Yulin, and D. V. Skryabin, “Solitons and frequency combs in silica microring resonators: Interplay of the Raman and higher-order dispersion effects,” *Phys. Rev. A* **92**, 033851 (2015).
  - [8] K.J. Blow and D. Wood, “Theoretical description of transient stimulated Raman scattering in optical fibers,” *IEEE J. Quantum Electron.* **25**, 2665 (1989).